International Journal of Applied Ceramic Technology

RESEARCH ARTICLE OPEN ACCESS

Microstructural Engineering of Sodium Potassium Niobate for Enhanced and Temperature-Stable Electromechanical Response

Andraž Bradeško[1] | Janina Roknić[1,2] | Nejc Suban[1,2] | Katarina Žiberna[1] | Silvo Drnovšek[1] | Brigita Kmet[1] | Aadil Abass Shah[1] | Marko Robić[1] | Hana Uršič[1,2] | Tadej Rojac[1,2] | Andreja Benčan Golob[1,2] | Barbara Malič[1,2]

[1]Jožef Stefan Institute, Ljubljana, Slovenia | [2]Jožef Stefan International Postgraduate School, Ljubljana, Slovenia

Correspondence: Andraž Bradeško (andraz.bradesko@ijs.si) | Barbara Malič (barbara.malic@ijs.si)

Received: 27 March 2026 | **Revised:** 17 April 2026 | **Accepted:** 30 April 2026

Keywords: ferroelectric| lead-free| piezoelectric| transducers| ultrasonic

ABSTRACT

The development of high-performance lead-free piezoelectrics is a critical step toward sustainable electronic components, yet matching the electromechanical stability over external variables, such as temperature, of lead-based standards remains a significant challenge. This study investigates the synergistic effects of Ti-doping and $K_{5.4}Cu_{1.3}Ta_{10}O_{29}$ (KCT) co-modification on the structural and functional properties of $(K_{0.5}Na_{0.5})NbO_3$ (KNN) ceramics. Co-modification significantly enhances both electromechanical coupling and the mechanical quality factor, parameters essential for ultrasonic transducer applications. A comparative analysis of the ferroelectric behavior reveals that these modifications establish a stable internal bias field leading to the hardening of piezoelectric properties. Interestingly, the samples modified solely by Ti exhibit a stronger internal bias field than the Cu-containing co-modified samples, a phenomenon further explored through domain imaging. When benchmarked against commercial hard PZT, the optimized KNN-Ti-KCT ceramic demonstrates comparable thermal stability in the room-temperature to 100°C range. Although a trade-off exists between peak piezoelectric coefficients and environmental impact, these results highlight the potential of tailored KNN ceramics as reliable lead-free alternatives for high-temperature electromechanical devices.

1 | Introduction

Ferroelectric materials are used in a broad range of applications, including sensors, actuators, energy harvesters, MEMS devices, and transducers [1]. Material properties that condition their successful integration in devices include electromechanical response, electrical loss, and mechanical quality factor. The properties are inherently antagonistic; improving one often comes at the expense of the other. As a result, material selection and optimization must strike a balance tailored to the application's specific requirements.

The most prominent piezoelectric ceramic, $Pb(Zr,Ti)O_3$ (PZT), possesses superior and tunable properties [2]; however, it contains toxic lead, making its processing hazardous to humans and the environment. Alternative materials are being developed and researched, with the most promising being barium-titanate-based, bismuth-sodium-titanate-based, bismuth-ferrite-based, and sodium-potassium-niobate-based materials.

One of the most promising and investigated compositions is $(K_{0.5}Na_{0.5})NbO_3$ (KNN) exhibiting a piezoelectric d_{33} coefficient

in the range of 100 pC/N. KNN is difficult to sinter, which leads to problems with high conductivity, hygroscopicity, and low responsivity [3]. Several approaches have been introduced to improve KNN properties, ranging from chemical modification to microstructural texturing. Microstructural engineering is a possible path to tackle the properties of KNN ceramics [4, 5]. Matsubara et al. [6] modified the KNN with the $K_{5.4}Cu_{1.3}Ta_{10}O_{29}$ (KCT) sintering aid. The role of KCT is multifold; it (i) stimulates liquid-assisted sintering, (ii) inhibits grain growth, and (iii) provides an excess of B-site ions. The KCT addition modifies the electromechanical and electrical response of the material. As shown by Zeng et al. [7], reduced grain size (GS) can alter the domain dynamics. They demonstrated that in KNN, fine grains contain predominantly 180° domain walls as a result of the grain-boundary-induced stress. Fine-grained ceramics exhibit high coercive fields and slow domain growth rates. In contrast, non-180° domain walls, which facilitate domain wall dynamics, are characteristic of coarse-grained ceramics. They possess lower coercive fields and higher domain growth rates. The grain-size effect is also directly reflected in the piezoelectric response, as shown for KNN with GSs from 0.8 to 2 μm [8] and other material systems [9].

Azadeh et al. [10] systematically studied the chemical modification of KNN by doping it with Ca and Fe. Ca occupies A-sites of the perovskite lattice, thereby serving as a donor dopant. In classical ferroelectrics, donor doping softens the ferroelectric response, evidenced by an increased ease of polarization reversal under applied external fields. However, it was shown that Ca does not have a pronounced softening effect in KNN. On the other hand, Fe occupies B-sites of the perovskite lattice and is a typical acceptor dopant. Acceptor doping is associated with hardening of ferroelectric properties, that is, increased difficulty of polarization. The authors showed that oxygen vacancies are the predominant conducting species at elevated temperatures. They calculated the activation energy for electrical conductivity, which was close to 1 eV, a value typical of thermally activated oxygen vacancy migration. Cu is an acceptor dopant in KNN ceramics sintered in oxidizing conditions, while sintering in reducing conditions results in Cu occupying the A-site position, as revealed by density functional theory (DFT) simulations [11]. Later, several studies confirmed that Cu occupies Nb sites in the KNN lattice and acts as a hard dopant. Eichel et al. [12] showed that upon Cu doping of KNN, trimer and dimer defect complexes form in equal concentrations:

$$[\left(Cu''''_{Nb} - V^{\cdot\cdot}_{O}\right)'] \approx [(V^{\cdot\cdot}_{O} - Cu''''_{Nb} - V^{\cdot\cdot}_{O})^{\cdot}] \quad (1)$$

The former contain electric and elastic dipoles, whereas the latter possess only elastic dipoles due to their linear, symmetric configuration. This consequently implies that, to switch the orientation of the defect complex, two oxygen vacancies must move, thereby increasing the energy required for reorientation. This results in an exceptionally high mechanical quality factor ($Q^{p}{}_{m}$) of Cu-doped KNN [13, 14].

Ti is another acceptor dopant in KNN. At 0.5 mol% Ti, the densification is promoted and dielectric loss is decreased compared to undoped KNN [15]. Cheng et al. studied the influence of Ti doping at 0.5–2 mol% on densification and grain growth. With increasing Ti concentration in KNN, the relative density increases, the GS decreases, and the GS distribution narrows. At 0.5 mol% Ti, a bimodal GS distribution evolves, interpreted as an intermediate state between the coarse cuboidal grains of the undoped KNN and fine-grained doped formulation. The coexistence of coarse and fine grains mitigates intergranular stress, which arises from grain misorientation, and enhances piezoelectric performance and the breakdown strength [16].

In our study, we systematically investigate the synergistic effects of chemical modification on the structural and functional properties of KNN ceramics. Specifically, we compare the dielectric, ferroelectric, and electromechanical responses of Ti-doped KNN and KNN, co-modified with both Ti and KCT. Our results demonstrate that Ti doping at 0.1 mol% induces a skewed grain-size distribution and yields modest piezoelectric properties (d_{33} = 20 pC/N). The addition of KCT at 0.38 mol% significantly improves the planar electromechanical coupling factor (k_p) and the planar mechanical quality factor ($Q^{p}{}_{m}$), which are critical parameters for high-power ultrasonic applications. Finally, we evaluate the thermal stability of the KNN-Ti-KCT between room temperature and 100°C and benchmark its performance against a commercial hard PZT ceramic. Although the co-modified KNN exhibits superior temperature stability relative to the commercial reference, this robustness comes at the cost of a lower piezoelectric coefficient d_{33}, highlighting a key design trade-off for lead-free alternatives in high-temperature environments.

2 | Methods

$K_{0.5}Na_{0.5}Nb_{0.99}Ti_{0.01}O_{2.995}$ (KNN-Ti) and $K_{5.4}Cu_{1.3}Ta_{10}O_{29}$ (KCT) powders were prepared separately by a conventional solid-state route from K_2CO_3 (Chempur, 99.9%), Na_2CO_3 (Chempur, 99.9%), Nb_2O_5 (Aldrich, 99.9%), Ta_2O_5 (Alfa Aeser, 99.85%), TiO_2 (Alfa Aeser, 99.8%), and CuO (Alfa Aeser, 99.7%) following the procedure described in our prior work [17]. The reagents were dried at 200°C for 24 h to remove moisture. The dried powders were weighed in stoichiometric ratios in a dry box under a nitrogen atmosphere. The powder mixtures corresponding to the KNN-Ti and KCT formulations were homogenized in a planetary mill using a 250 mL ZrO_2 vial and 3 mm diameter yttria-stabilized zirconia (YSZ) milling balls at 200 1/min for 4 h, with isopropanol, then dried at 105°C, sieved through a 300 μm sieve, and dried at 200°C.

For the solid-state synthesis of KNN-Ti, the powder was uniaxially pressed at 50 MPa into a 20 mm diameter pellet. The sample was heated twice at 800°C for 4 h in a closed alumina crucible on a platinum foil. After both heating steps, the pellet was crushed and milled in a planetary mill at 200 1/min for 4 h using the same vessel and milling balls as for homogenization. The median particle size of KNN-Ti was 0.40 μm, determined by laser granulometry.

The KCT powder was synthesized by heating the reagent powder mixture uniaxially pressed into a pellet at 50 MPa at 900°C for 4 h, followed by milling, yielding a median particle size of 0.60 μm. In all cases, the heating and cooling rates were 5 K/min with an intermediate step at 200°C for 2 h.

The mixture of KNN-Ti and KCT powders in a 0.9962/0.0038 molar ratio, abbreviated as KNN-Ti-KCT, was homogenized in a planetary mill at 200 1/min for 2 h.

The synthesized powders were sieved, dried at 200°C, and stored in a dry atmosphere.

The powder compacts were shaped by uniaxial and isostatic pressing at 100 and 300 MPa, respectively. Sintering was performed in air at 1100°C for 2 h, with heating and cooling rates of 2 K/min, in closed alumina crucibles.

The phase composition of the powdered samples was analyzed by x-ray diffraction with Cu-$K\alpha$ radiation over the 2θ range 10°–70° with a step size of 0.01° (XRD, MiniFlex 600-C Rigaku). The density of the sintered samples was determined by helium pycnometry (Accu Pyc II 1340, Micromeritics) and calculated from mass and dimensions. The ceramic samples were ground and polished using standard ceramographic techniques. The polished sections were thermally etched to reveal the grain boundaries. A field-emission scanning electron microscope (FE-SEM JEOL JSM-7600) with an energy-dispersive x-ray spectrometer (EDXS, INCA Oxford 350 EDS SDD) was used to analyze the microstructure. The imaging was performed at an accelerating voltage of 15 kV using the backscattered-electrons detector (BSE). The GS was determined from SEM micrographs of the microstructures, which were processed with ImageJ by measuring approximately 800 grains for KNN-Ti and 300 grains for KNN-Ti-KCT. The evaluated grains were expressed as the mean Feret diameter. Electron-transparent lamellas were prepared using a gallium source focused ion beam (Helios Nanolab 650 HP, Thermo Fisher Scientific). An aberration-corrected scanning transmission electron microscope (STEM) (Spectra 300, Thermo Fisher Scientific) equipped with Super-X G2 EDXS detector (Thermo Fisher Scientific) was used to study the chemical composition at the nanoscale.

Atomic force microscopy (AFM) and piezoresponse force microscopy (PFM) analyses were performed using an atomic force microscope (MFP-3D, Asylum Research, Santa Barbara, CA, USA) equipped with a high-voltage PFM module. Prior to the sample investigation, the sample surfaces were prepared using standard metallographic procedures, as detailed in Ref. [18]. For PFM imaging, Ti/Ir-coated silicon tips (ASYELEC.01-R2, Oxford Instruments, UK) with a nominal tip radius of 25 nm and resonance frequency of 75 kHz were used. Out-of-plane PFM amplitude and phase images were recorded in dual AC resonance tracking (DART) mode by applying an AC voltage of 3 V amplitude at a frequency of ≈290 kHz to the samples.

The commercial PIC144 had silver electrodes and the disc sample had a diameter of 10 mm and thickness of 1 mm. The samples had DC sputtered Au electrodes (5 Pascal, Italy), except for the high temperature dielectric measurements (>400°C) where screen printed Au electrodes were used. The samples used for impedance measurements at resonance had a diameter of 10 mm and thickness of 0.7 mm.

Room-temperature polarization versus electric field (P–E) hysteresis loops were determined using an Aixacct TF analyzer 2000 with a sinusoidal driving voltage of 10 Hz.

KNN-Ti was poled at room temperature at 30 kV/cm and 30 min, KNN-Ti-KCT was poled at 120°C for 30 min with 30 kV/cm and field-cooled.

The impedance analyzer (Bode100, Omicron, Germany) was used to measure the impedance spectra in the frequency range of 10 kHz to 40 MHz. The excitation voltage was limited to 200 mV. The LCR analyzer (IM3536, Hioki, Japan) and impedance analyzer (Solatron, 1260A, United Kingdom) were used to evaluate the capacitance and impedance of the samples as a function of temperature.

The Berlincourt piezometer (PM300, Piezotest, Singapore) was used to measure the piezoelectric coefficient; the static force was 10 N, the dynamic force was 0.25 N, and the excitation frequency was 110 Hz.

3 | Results

3.1 | KNN-Ti Ceramics

Upon sintering at 1100°C, KNN-Ti crystallizes in the perovskite phase (Figure S1) and reaches a density of 4.38 g/cm^3 (relative density of 97%). Ti-doping enhances densification relative to undoped KNN, which is consistent with prior studies [15, 16].

The microstructure of KNN-Ti ceramic is presented in the SEM micrograph in Figure 1a. Some bright second-phase (Figure 1a, red arrows) inclusions are evident in the back-scattered image, indicating an alkali-deficient phase [19]. Thermal etching was implemented to expose the grain boundaries (Figure 1b). The broad, skewed GS distribution is clearly illustrated by coloring the grains according to their Feret's diameters, see Figure 1c. Large, faceted grains (red) coexist with clusters of significantly finer grains (blue), supporting the inhomogeneous grain boundary mobility upon low-concentration Ti-doping as proposed by Cheng et al. [16]. Still, we cannot exclude the possibility that such a nonuniform microstructure is due to the nonhomogeneous distribution of 0.1 mol% of Ti-dopant in the KNN matrix, notwithstanding two calcination steps with intermediate milling. The GS distribution plot is shown in Figure 1d. The median GS is (1.53 ± 1.59) μm, and the distribution shows a tail spanning to the Feret diameter of 12 μm.

We note that coarse, angular grains exhibit visible internal striations, characteristic of ferroelectric domain patterns.

The ferroelectric response of the KNN-Ti ceramic is evaluated through polarization–electric field (P–E) hysteresis measurements, as shown in Figure 2. The sample exhibits a pinched and shifted hysteresis loop, characteristic of a significant internal bias field (E_{ib}). Specifically, the negative and positive coercive fields are at $E_{C1} = -8.3$ kV/cm and $E_{C2} = 19.5$ kV/cm, respectively. These values yield an average coercive field E_C of 13.9 kV/cm and a calculated E_{ib} of 5.6 kV/cm. The polarization does not saturate, reaching a maximum value (P_{max}) of approximately 16 μC/cm^2, whereas the remanent polarization P_r is 7 μC/cm^2. The current density–electric field (j–E) characteristics, represented by the dashed lines, show distinct peaks that correspond to the switching of ferroelectric domains, confirming that the

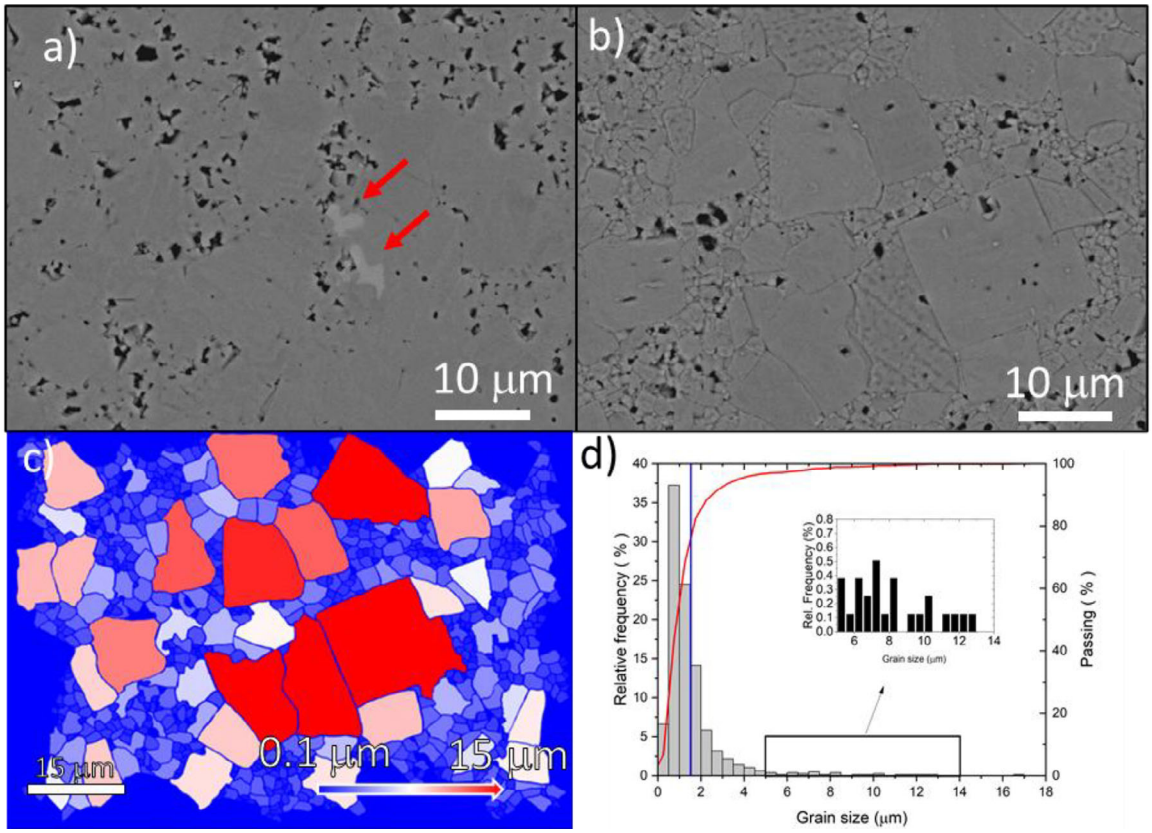

FIGURE 1 | (a) SEM micrograph of the polished KNN-Ti surface. Red arrows point to alkali-deficient phase. (b) SEM micrograph of the thermally etched surface with visible grains and grain boundaries. (c) Etched microstructure showing the distribution of grain sizes according to the color scale from 0.1 µm (blue) to 15 µm (red). (d) Histogram of grain sizes. The blue vertical line shows median grain size, whereas the red curve shows the cumulative passing percent of grains at a certain value.

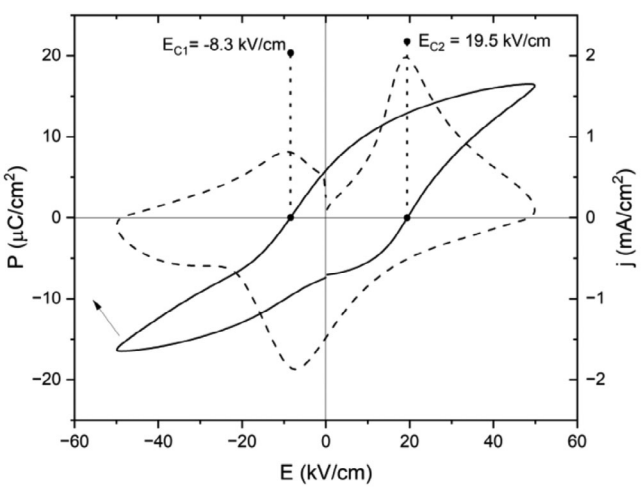

FIGURE 2 | Polarization–electric field (P–E) and current–electric field (j–E) loops of KNN-Ti at 10 Hz. The E_{C1} and E_{C2} show the intercept of the polarization curve with the E-field axis. The full line shows the polarization, and the dashed line shows the electric current density.

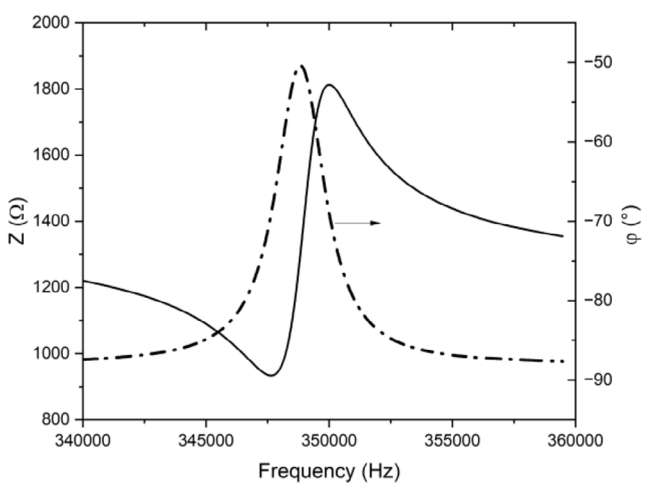

FIGURE 3 | Impedance magnitude (Z) and phase angle (φ) at planar resonance mode. The dashed line corresponds to the phase and the full line to impedance.

observed polarization arises from the switching rather than just a lossy dielectric [20]. The P–E loop exhibits a notably slanted profile, which suggests a broad distribution of switching fields within the material [21]. This behavior can be attributed to the broad GS distribution and the resulting intergranular stresses. In larger grains, domain switching is facilitated by lower localized stresses, allowing easier alignment under the applied field and thus a lower E_C. In contrast, smaller grains experience higher mechanical constraints and larger intergranular stresses that hinder domain wall motion, requiring higher field amplitudes to achieve switching [7, 22]. A further increase in the excitation

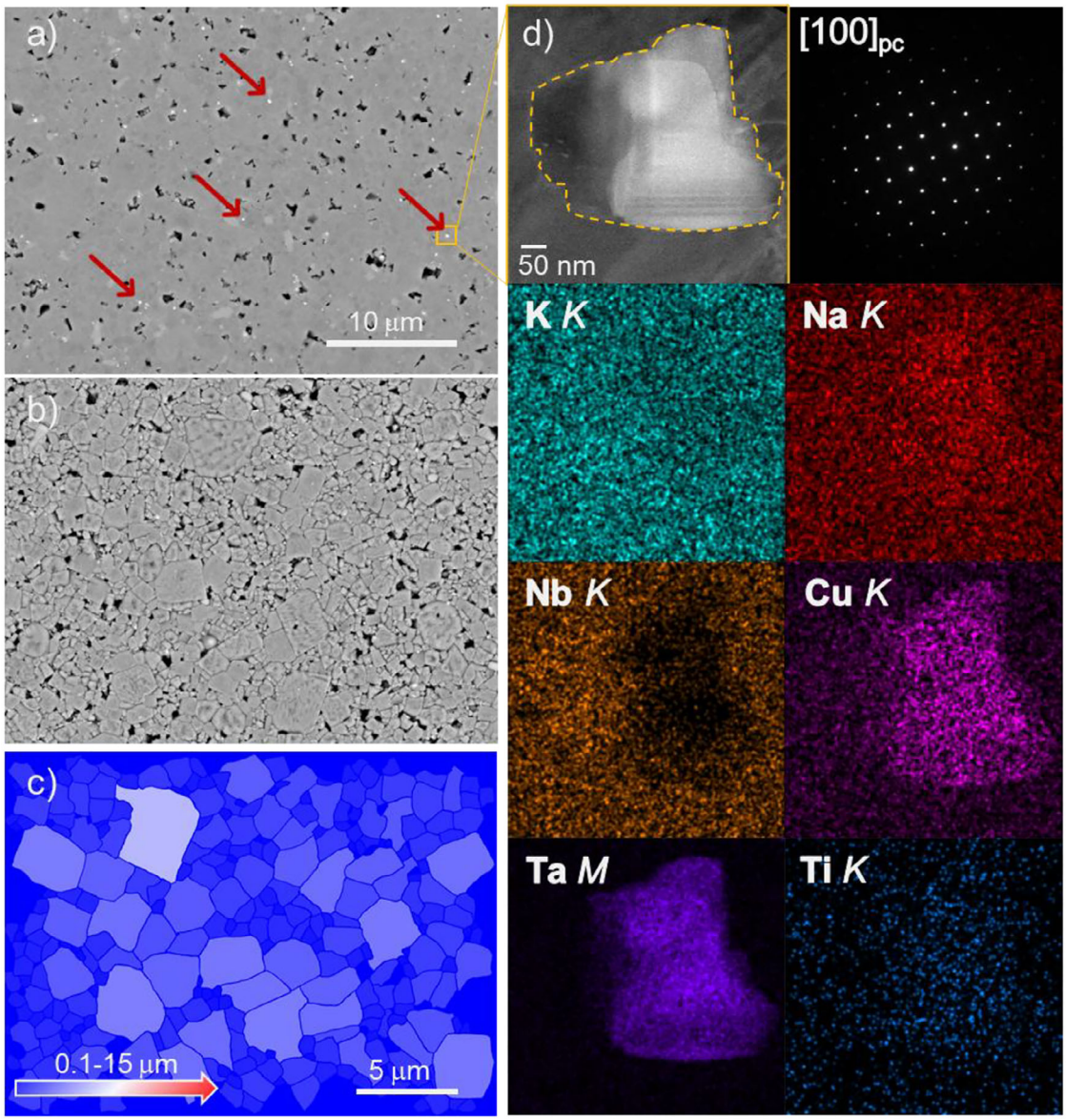

FIGURE 4 | (a) SEM micrograph of the polished KNN-Ti-KCT surface. (b) SEM micrograph of the thermally etched surface with visible grains and grain boundaries. (c) Microstructure showing the distribution of grain sizes according to the color scale from 0.1 µm (blue) to 15 µm (red). (d) STEM image of the Ta- and Cu-rich inclusion within the grain in the [1 0 0] pseudo-cubic zone axis, together with the corresponding selected area diffraction pattern and elemental mapping. The EDXS analysis shows Ta and Cu rich area, while simultaneously showing Nb deficiency.

voltage leads to increased leakage current, ultimately resulting in sample breakdown.

Due to high leakage currents at elevated temperatures, samples were poled at RT. The relative permittivity of the poled KNN-Ti at 1 kHz and 1 V is 385 with a tanδ of 0.015. The d_{33} coefficient is 20 pC/N. The electromechanical coupling behavior was further investigated by the frequency dependence of the impedance and phase angle in the planar vibration mode, see Figure 3. The sample exhibits a typical resonance–antiresonance characteristic, necessary for determining the electromechanical coupling factor. The characteristic resonance frequency (f_r), corresponding to the minimum impedance, is at 347.5 kHz, whereas the antiresonance frequency (f_a), corresponding to the maximum impedance, is at 350.1 kHz. The bandwidth of approximately 2.6 kHz results in a planar electromechanical coupling factor (k_p) of approximately 0.14. This value indicates low electromechanical coupling, consistent with the slanted hysteresis behavior observed in Figure 3. The mechanical quality factor $Q^p{}_m$ is below 100. The phase angle reaches a maximum of approximately −52°, failing to cross into the inductive region. This suggests a high level of internal damping and dielectric loss, likely a direct consequence of incomplete poling and a broad GS distribution, which broadens the resonance response and increases mechanical energy dissipation.

3.2 | KNN-Ti-KCT Ceramics

KCT was introduced into the KNN-Ti matrix as a chemical modifier and sintering aid, as reported in earlier studies [6]. KNN-Ti-KCT ceramic has a density of 4.45 g/cm^3 (relative density of 98%, assuming the theoretical density of undoped KNN) after

sintering at 1100°C, indicating enhanced densification of the KNN-Ti matrix by the KCT addition. The ceramic crystallizes in the orthorhombic perovskite phase (see Figure S1). Additional low-intensity peaks are assigned to the $K_{5.4}Cu_{1.3}Ta_{10}O_{29}$ phase (PDF 00-043-0334).

The microstructure of KNN-Ti-KCT is shown in Figure 4. The polished surface reveals the presence of secondary phases. We assume that the light grey ones are alkali-deficient polyniobates, similar to those observed in KNN-Ti [19].

The median GS of the ceramic is (0.96 ± 0.59) μm, indicating a strong reduction of the GS and inhibition of the skewed GS distribution (histogram shown in Figure S2). KCT thus acts as a potent inhibitor of abnormal grain growth. The distribution of Feret diameters using the same color scale as Figure 1 clearly demonstrates a more uniform GS distribution as in KNN-Ti (see Figure 1c and compare with Figure 4c).

Very bright, high-contrast precipitates are indicated by red arrows in the polished and thermally etched microstructure (Figure 4a,b). Their high brightness in a backscattered electron mode SEM imaging indicates a higher atomic number, probably the presence of Ta. A Ta-rich secondary phase was observed in the microstructure of $(K_{0.49}Na_{0.49}Li_{0.02})(Nb_{0.8}Ta_{0.2})O_3$ (KNLNT) ceramics by Condurache et al. [23]. STEM-EDXS analysis (Figure 4d) confirmed that the inclusions are Ta-rich and possibly Cu-rich. The observed Nb deficiency suggests that Ta and Cu ions substitute for Nb in the perovskite lattice. However, Cu signals in STEM can also arise from the microscope environment (e.g., Cu grid and detector components), making it difficult to determine how much Cu originates from the specimen itself. Similarly, apparent Na enrichment in secondary phases may be an artifact of local variations in the Cu signal rather than true compositional differences.

The localized presence of Ta-rich inclusions at the grain boundaries possibly provides a Zener pinning effect that restricts grain growth [24–26]. Thus, the combination of Ti-doping and KCT addition produces a refined and stabilized microstructure. The addition of KCT suppresses the abnormal grain growth observed in the Ti-doped sample, resulting in a homogeneous, fine-grained microstructure, which is essential for optimizing the ferroelectric, piezoelectric, and dielectric properties.

The ferroelectric behavior of the KNN-Ti-KCT ceramic shows a significant enhancement in polarization relative to KNN-Ti, with saturation (P_{sat}) at approximately 28 μC/cm^2 (Figure 5). KNN-Ti-KCT exhibits asymmetric coercive fields of $E_{C1} = -8.3$ kV/cm and $E_{C2} = 14.5$ kV/cm, resulting in an average coercive field of 11.4 kV/cm and internal bias field E_{ib} of 3.1 kV/cm. A comparison between KNN-Ti and KNN-Ti-KCT reveals distinct differences in the magnitude of the coercive field shift. In general, the respective shift is typically attributed to the alignment of defect dipoles. Given that Cu (stemming from the KCT additive) acts as an acceptor dopant in KNN, we expected that KNN-Ti-KCT would have a more pronounced internal bias than KNN-Ti due to the formation of dimer and trimer defect complexes (Equation 1). However, KNN-Ti exhibits a higher internal bias ($E_{ib} = 5.6$ kV/cm) than KNN-Ti-KCT-($E_{ib} = 3.1$ kV/cm), suggesting that the effect of Ti-substitution on defect formation creates a more robust internal

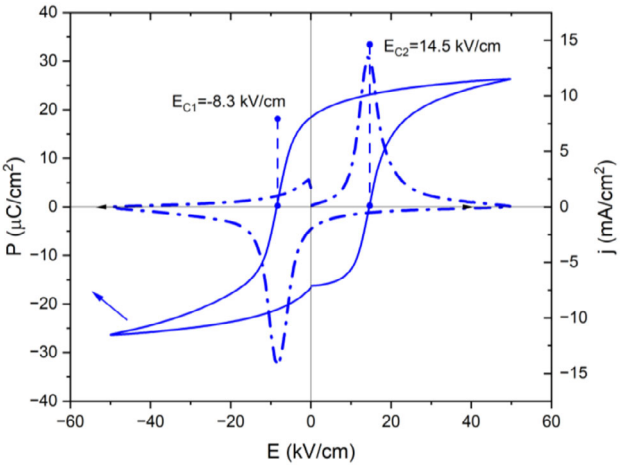

FIGURE 5 | Polarization–electric field (P–E) and current–electric field (j–E) loops of KNN-Ti-KCT at 10 Hz. The E_{C1} and E_{C2} show the intercept of the polarization curve with the E-field axis. The full line shows polarization and dashed electric current density.

bias field than the addition of KCT. Another factor influencing the internal bias could be GS and GS distribution, which is much larger and broader in KNN-Ti than in KNN-Ti-KCT, namely, (1.53 ± 1.59) μm versus (0.96 ± 0.59) μm.

To understand why the pinning force and the resulting internal bias are more pronounced in KNN-Ti than in KNN-Ti-KCT, the ferroelectric domain structures of both KNN-Ti and KNN-Ti-KCT samples were investigated using PFM. AFM topography-height images and PFM out-of-plane amplitude and phase images of KNN-Ti and KNN-Ti-KCT are shown in Figure 6. In the KNN-Ti sample (Figure 6b), coarse lamellar ferroelectric domains (highlighted by the green dotted rectangle) and wedge-shaped ferroelectric domains (highlighted by the red solid rectangle) are observed. Upon the introduction of KCT, both the GS and ferroelectric domain structure of the sample undergo drastic refinement. The KNN-Ti-KCT grains are smaller, and therefore the domain structure inside the grains is finer, the domains are more fragmented, and more irregular in shape, but still some smaller lamellar and wedge domains are also present (Figure 6e). Further details on the ferroelectric domain structures in both KNN-Ti and KNN-Ti-KCT samples, including higher magnification images, are provided in Figures S3 and S4. The larger internal bias in KNN-Ti is likely attributed to the larger domain size, which produces a longer range effect of defect complexes on the polarization state compared to the KNN-Ti-KCT. In the latter material, despite the presence of Cu as a strong acceptor dopant, the defect complexes are effective over a shorter range. This is due to the smaller GS and the resulting smaller ferroelectric domain sizes, which lead to the observed lower internal bias [27].

Poled KNN-Ti-KCT sample exhibits a d_{33} coefficient of 105 pC/N, which is in line with the literature [28]. The room-temperature impedance measurement at the planar resonance is shown in Figure 7a. The impedance shows a minimum and a maximum corresponding to the resonance and antiresonance frequencies. The phase angle between f_r and f_a is 89°. The k_p of 0.4 is almost three times that of KNN-Ti (0.14). The $Q^p{}_m$ of the KNN-Ti-KCT sample is 1100, about ten times that of KNN-Ti (<100). The very

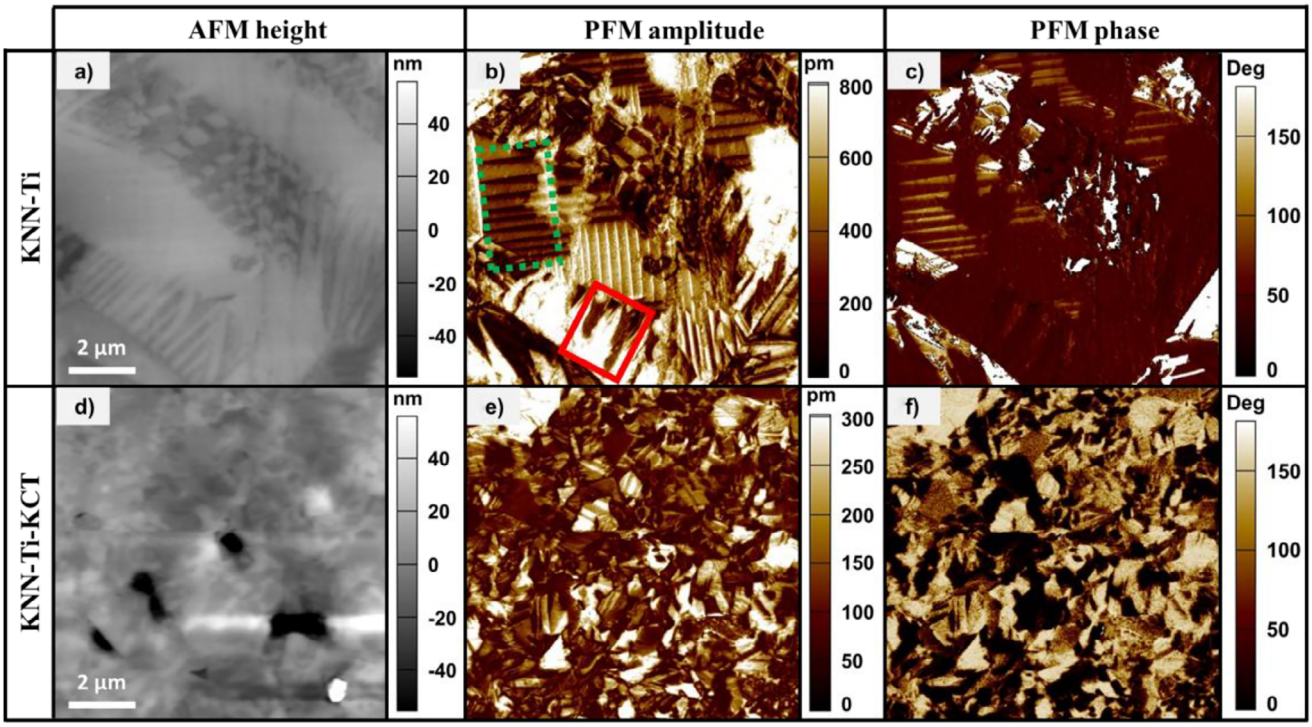

FIGURE 6 | AFM (a and d) topography-height images; PFM (b and e) amplitude and (c and f) phase images for KNN-Ti and KNN-Ti-KCT samples, respectively. Lamellar and wedge-shaped ferroelectric domains are indicated by green dotted and red solid rectangles in panel (b), respectively. Panels (a–c) correspond to the KNN-Ti sample, whereas panels (d–f) correspond to the KNN-Ti-KCT sample. AFM, atomic force microscopy; PFM, piezoresponse force microscopy.

high $Q^{p}{}_{m}$ of KNN-Ti-KCT indicates low mechanical loss in the ceramic, consistent with the high degree of poling, as evidenced by the phase angle reversal of 89° at resonance. Overall, the enhanced values of $Q^{p}{}_{m}$, phase angle, P_R, and P_{sat} indicate a higher degree of domain mobility and a narrower switching field distribution than in KNN-Ti.

The impedance response in planar and thickness modes was analyzed in detail to determine the electrical, elastic, and electromechanical parameters of KNN-Ti-KCT. Figure 7b shows the thickness mode resonance of KNN-Ti-KCT. The evaluation of the thickness-mode bandwidth enables determination of the thickness-mode electromechanical coupling factor. By using models developed by several authors (see Refs. [2, 29–31]), the d_{31}, c_{33}, k_{33}, and k_{31} were estimated by a custom analysis script available in Ref. [32]. The data are collected in Table 1.

The piezoelectric coefficients of KNN-Ti-KCT are lower than those of commercial hard PZT (PIC144, d_{33} = 300 pC/N, Table 1) and the best KNN compositions reported in the literature (up to 570 pC/N in Ref. [33]) [34]. The stiffness coefficient s_{33} is 12.4×10^{-12} m^2/N, which is smaller than the values typically measured in commercial PZT (i.e., 14.3×10^{-12} m^2/N) and comparable to the values in the literature [35]. Moreover, low mechanical and electrical losses, as well as response stability, are often required in applications. Thus, we analyzed the temperature dependence of the dielectric and transducer properties of KNN-Ti-KCT.

The dielectric properties of unpoled KNN-Ti-KCT sample as a function of temperature are shown in Figure 8. The orthorhombic

TABLE 1 | Measured and calculated properties of KNN-Ti-KCT.

	KNN-Ti-KCT	PIC144	unit
ε_{33}	290	1300	/
tanδ	0.003	0.003	/
d_{33}	105	300	pC/N
d_{31}	−35	−140	pC/N
$s^{E}{}_{33}$	12.4	14.3	10^{-12} m^2/N
$s^{E}{}_{11}$	8	12.4	10^{-12} m^2/N
$Q^{p}{}_{m}$	1069	1000	/
k_p	0.40	0.60	/
k_t	0.45	0.48	/
k_{33}	0.58	0.66	/
k_{31}	0.24	0.30	/

Note: PIC144 properties were taken from the PI ceramic GmbH datasheet [36].

to tetragonal phase transition temperature (T_{o-t}) and the Curie point are at 188°C and 382°C, respectively. We note that the phase transition temperatures of KNN-Ti-KCT are lower than the respective temperatures of KNN-Ti (Figure S5, T_C = 397°C) and KNN (Figure S6, T_C = 419°C), indicating the incorporation of Cu and Ta into the perovskite matrix.

The inset illustrates the low and stable tanδ over the temperature range from RT to 100°C. The exceptionally low losses, in our case

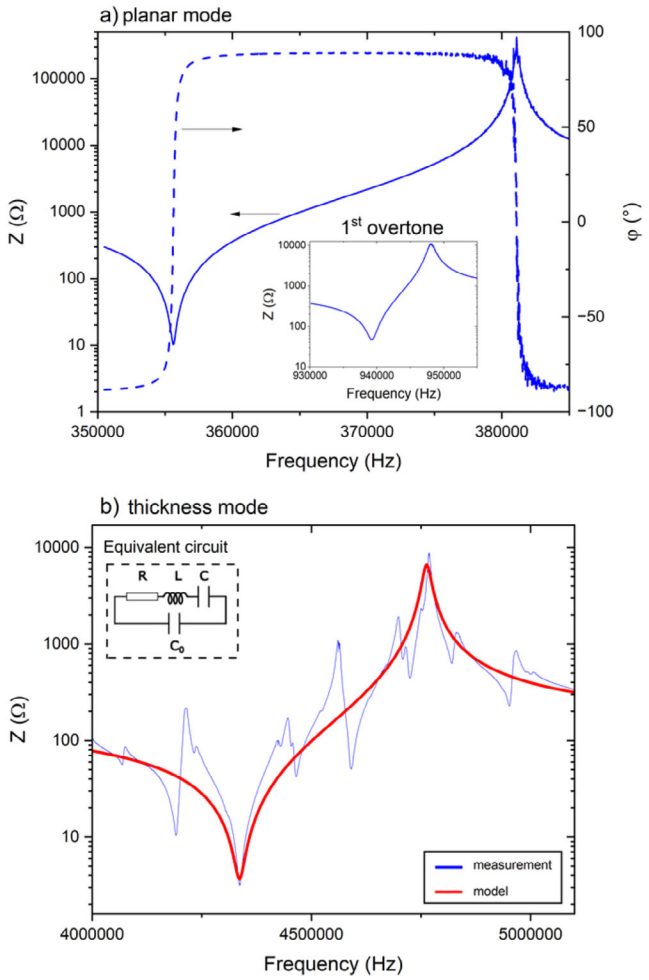

FIGURE 7 | Impedance magnitude (Z) and phase angle (φ) at planar and thickness mode resonance. (a) Impedance magnitude (Z) and phase angle (ϕ) at planar mode resonance. The dashed line corresponds to the phase and the full line to impedance. The inset shows the impedance of the first overtone of the planar mode. (b) The blue full line shows the measurement, and the red full line the modeled response. The inset shows the equivalent circuit model used to model the response. R is the resistance, L is the inductance, C is the capacitance, and C_0 is the free capacitance of the sample.

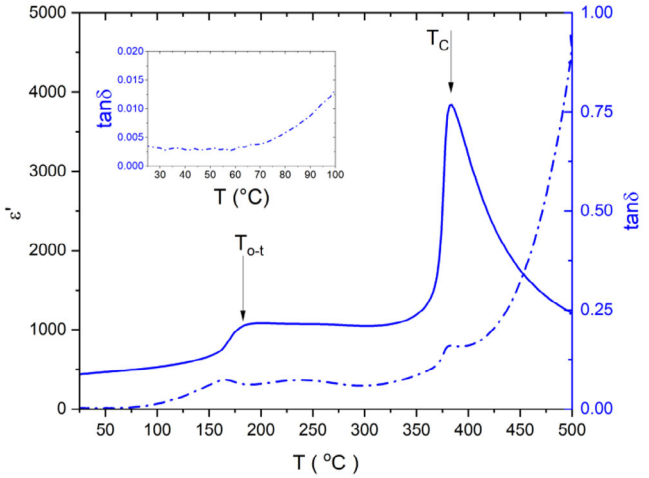

FIGURE 8 | Dielectric permittivity (ε') and loss ($\tan\delta$) of KNN-Ti-KCT as a function of temperature at 1 kHz. The inset shows the dielectric loss in the temperature ranges from RT to 100°C. T_{o-t} denotes the temperature of the orthorhombic to tetragonal transition and T_C the Curie point.

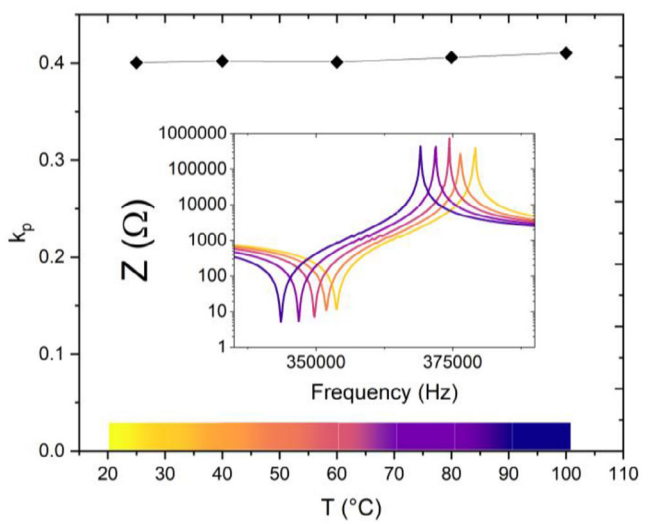

FIGURE 9 | Electromechanical coupling coefficient (k_p) of KNN-Ti-KCT as a function of temperature. The inset shows impedance magnitude spectra at planar resonance mode for various temperatures.

below 0.005 at RT, are important for transducer applications, as they preclude self-heating and depoling issues [37]. Over the same temperature range, the dielectric permittivity steadily increases by 20% relative to the RT value, from 442 to 529. In KNN-Ti, the increase is 29%, and in the hard ferroelectric PIC144, it is 20% (Figure S7). We conclude that the response of KNN-Ti-KCT is stable relative to a commercial hard PZT.

The temperature dependence of the planar electromechanical coupling factor k_p for KNN-Ti-KCT is presented in Figure 9. The electromechanical performance remains almost constant over a broad temperature range, from RT to 100°C, which is critical for high-temperature piezoelectric applications. The inset displays the impedance magnitude (Z) as a function of frequency, highlighting a well-defined planar resonance at all temperatures. The k_p varies by 2% over the range from RT to 100°C, compared with 5% for the commercial ceramic PIC144 (see Figure S8). The slight fluctuations in k_p observed in the plot are attributed to changes in domain wall mobility and the temperature-dependent relaxation of the internal bias field (E_{ib}), which was previously identified in the P–E loop (cf. Figure 5).

4 | Conclusions

In this work, the structural and electromechanical properties of Ti- and KCT-modified KNN ceramics were systematically investigated. We found that the addition of a secondary KCT phase leads to significant grain fragmentation, resulting in a refined microstructure compared to Ti-doped KNN. This reduction in GS is directly correlated with a transition to smaller ferroelectric domains. A key observation of this study is that the effectiveness

of "hardening" through defect-mediated pinning is GS dependent and constrained by the characteristic length scales of the domain morphology. The results indicate that the degree of "hardening" in lead-free ceramics is not solely dictated by the presence of acceptor dopants. Instead, the long-range order and crystallinity of the ceramic matrix play a decisive role in defining how effectively these dopants can affect the polarization dynamics under an electric field.

The co-modified KNN-Ti-KCT system exhibits exceptionally low mechanical and electrical losses. Furthermore, this composition demonstrates superior thermal stability in the planar electromechanical coupling factor (k_p), dielectric loss (tanδ), and permittivity (ε'), maintaining performance consistency across a broad temperature range.

Ultimately, the electromechanical performance in ceramics is the result of a complex interplay between GS, localized stress gradients, internal electric fields, and defect-mediated domain dynamics. These factors must be tuned to engineer high-performance lead-free piezoelectrics.

Acknowledgments

This research was funded by the European Union's 2022 Research and Innovation Program EDF-2022-RA SCUALE project under grant number 101121213, Slovenian Research Agency (research core funding P2-0105, including funding for young researchers J.R., K.Ž., and N.S.). Maria Clara de Morais (Erasmus+ program) is gratefully acknowledged for her help in the laboratory.

Data Availability Statement

The data that support the findings of this study are openly available in Zenodo repository [38].

References

1. K. Uchino, *Ferroelectric Devices* (CRC Press, 2018), https://doi.org/10.1201/b15852.

2. B. Jaffe, W. R. Cook Jr., and H. L. Jaffe, *Piezoelectric Ceramics* (Elsevier, 1971), https://doi.org/10.1016/B978-0-12-379550-2.X5001-7.

3. J. Koruza, A. J. Bell, T. Frömling, K. G. Webber, K. Wang, and J. Rödel, "Requirements for the Transfer of Lead-Free Piezoceramics Into Application," *Journal of Materiomics* 4, no. 1 (2018): 13–26, https://doi.org/10.1016/j.jmat.2018.02.001.

4. B. Malič, J. Koruza, J. Hreščak, et al., "Sintering of Lead-Free Piezoelectric Sodium Potassium Niobate Ceramics," *Materials* 8, no. 12 (2015): 8117–8146, https://doi.org/10.3390/ma8125449.

5. B. Malič, "Sodium–Potassium–Niobate Based Piezoelectric Ceramics: Processing—Microstructure—Properties," *Japanese Journal of Applied Physics* 63 (2024): 100801, https://doi.org/10.35848/1347-4065/ad7862.

6. M. Matsubara, T. Yamaguchi, K. Kikuta, and S. I. Hirano, "Sintering and Piezoelectric Properties of Potassium Sodium Niobate Ceramics With Newly Developed Sintering Aid," *Japanese Journal of Applied Physics, Part 1: Regular Papers and Short Notes and Review Papers* 44, no. 1 A (2005): 258, https://doi.org/10.1143/JJAP.44.258.

7. F. Zeng, H. Huang, Z. Zhong, et al., "Microscopic Mechanisms of Grain Size Effects on Domain Switching in Sodium Potassium Niobate Ceramics," *Journal of Applied Physics* 138, no. 8 (2025): 084101, https://doi.org/10.1063/5.0273310.

8. S. Huo, S. Yuan, Z. Tian, C. Wang, and Y. Qiu, "Grain Size Effects on the Ferroelectric and Piezoelectric Properties of $Na_{0.5}K_{0.5}NbO_3$ Ceramics Prepared by Pechini Method," *Journal of the American Ceramic Society* 95, no. 4 (2012): 1383–1387, https://doi.org/10.1111/j.1551-2916.2011.04992.x.

9. J. Schultheiß, S. Checchia, H. Uršič, et al., "Domain Wall-Grain Boundary Interactions in Polycrystalline $Pb(Zr_{0.7}Ti_{0.3})O_3$ Piezoceramics," *Journal of the European Ceramic Society* 40, no. 12 (2020): 3965–3973, https://doi.org/10.1016/j.jeurceramsoc.2020.03.054.

10. M. Azadeh, C. Zhao, A. Pawadi, S. Gao, and T. Frömling, "Effect of Iron Acceptor Doping and Calcium Donor Doping in Potassium Sodium Niobate-Based Lead-Free Piezoceramics," *Journal of the American Ceramic Society* 107, no. 7 (2024): 4949–4961, https://doi.org/10.1111/jace.19803.

11. S. Körbel, P. Marton, and C. Elsässer, "Formation of Vacancies and Copper Substitutionals in Potassium Sodium Niobate Under Various Processing Conditions," *Physical Review B: Condensed Matter and Materials Physics* 81, no. 17 (2010): 174115, https://doi.org/10.1103/PhysRevB.81.174115.

12. R. A. Eichel, E. Erünal, P. Jakes, et al., "Interactions of Defect Complexes and Domain Walls in CuO-Doped Ferroelectric $(K,Na)NbO_3$," *Applied Physics Letters* 102, no. 24 (2013): 242908, https://doi.org/10.1063/1.4811268.

13. L. Cangini, H. Huang, C. Zhao, et al., "Hardening of $K_{0.5}Na_{0.5}NbO_3$ Piezoceramics With Cu and the Temperature Dependence in High-Power Drive," *Journal of Materiomics* 11, no. 3 (2025): 100962, https://doi.org/10.1016/j.jmat.2024.100962.

14. H. S. Han, J. Koruza, E. A. Patterson, et al., "Hardening Behavior and Highly Enhanced Mechanical Quality Factor in $(K_{0.5}Na_{0.5})NbO_3$–Based Ceramics," *Journal of the European Ceramic Society* 37, no. 5 (2017): 2083–2089, https://doi.org/10.1016/j.jeurceramsoc.2017.01.013.

15. X. Vendrell, J. E. García, X. Bril, D. A. Ochoa, L. Mestres, and G. Dezanneau, "Improving the Functional Properties of $(K_{0.5}Na_{0.5})NbO_3$ Piezoceramics by Acceptor Doping," *Journal of the European Ceramic Society* 35, no. 1 (2015): 125–130, https://doi.org/10.1016/j.jeurceramsoc.2014.08.033.

16. L. Q. Cheng, J. X. Liu, Y. Jiang, et al., "Fine-Grain Densification in Faceted Grain Ceramics via Chemical Modification," *Advanced Functional Materials* 36, no. 3 (2026): e12006, https://doi.org/10.1002/adfm.202512006.

17. B. Kmet, D. Kuščer, S. Dutta, et al., "Screen Printed Copper and Tantalum Modified Potassium Sodium Niobate Thick Films on Platinized Alumina Substrates," *Materials* 14, no. 23 (2021): 7137, https://doi.org/10.3390/ma14237137.

18. T. Rojac, H. Ursic, A. Bencan, B. Malic, and D. Damjanovic, "Mobile Domain Walls as a Bridge Between Nanoscale Conductivity and Macroscopic Electromechanical Response," *Advanced Functional Materials* 25, no. 14 (2015): 2099–2108, https://doi.org/10.1002/adfm.201402963.

19. B. Malic, D. Jenko, J. Holc, M. Hrovat, and M. Kosec, "Synthesis of Sodium Potassium Niobate: A Diffusion Couples Study," *Journal of the American Ceramic Society* 91, no. 6 (2008): 1916–1922, https://doi.org/10.1111/j.1551-2916.2008.02376.x.

20. J. F. Scott, "Ferroelectrics Go Bananas," *Journal of Physics: Condensed Matter* 20, no. 2 (2008): 021001, https://doi.org/10.1088/0953-8984/20/02/021001.

21. T. Schenk, E. Yurchuk, S. Mueller, et al., "About the Deformation of Ferroelectric Hystereses," *Applied Physics Reviews* 1, no. 4 (2014): 041103, https://doi.org/10.1063/1.4902396.

22. G. Arlt, "The Influence of Microstructure on The Properties of Ferroelectric Ceramics," *Ferroelectrics* 104, no. 1 (1990): 217–227, https://doi.org/10.1080/00150199008223825.

23. O. A. Condurache, K. Radan, U. Prah, et al., "Heterogeneity Challenges in Multiple-Element-Modified Lead-Free Piezoelectric Ceramics," *Materials* 12, no. 24 (2019): 4049, https://doi.org/10.3390/ma12244049.

24. Z. Li, H. C. Thong, Y. F. Zhang, et al., "Defect Engineering in Lead Zirconate Titanate Ferroelectric Ceramic for Enhanced Electromechanical Transducer Efficiency," *Advanced Functional Materials* 31, no. 1 (2021): 2005012, https://doi.org/10.1002/adfm.202005012.

25. C. Zhao, S. Gao, T. Yang, et al., "Precipitation Hardening in Ferroelectric Ceramics," *Advanced Materials* 33, no. 36 (2021): 2102421, https://doi.org/10.1002/adma.202102421.

26. F. Jean, F. Schoenstein, M. Zaghrioui, et al., "Composite Microstructures and Piezoelectric Properties in Tantalum Substituted Lead-Free $K_{0.5}Na_{0.5}Nb_{1-x}Ta_xO_3$ Ceramics," *Ceramics International* 44, no. 8 (2018): 9463–9471, https://doi.org/10.1016/j.ceramint.2018.02.163.

27. S. H. Teng, A. Dimou, B. Udofia, M. Ghasemi, M. Stricker, and A. Grünebohm, "Control of Ferroelectric Domain Wall Dynamics by Point Defects: Insights From Ab Initio Based Simulations," *Journal of Applied Physics* 137, no. 15 (2025): 154103, https://doi.org/10.1063/5.0259824.

28. S. Zhang, J. B. Lim, H. J. Lee, and T. R. Shrout, "Characterization of Hard Piezoelectric Lead-Free Ceramics," *Ieee Transactions on Ultrasonics, Ferroelectrics, and Frequency Control* 56 (2009): 1523–1527, https://doi.org/10.1109/TUFFC.2009.1215.

29. D. Damjanovic, "Highly Anisotropic Electromechanical Properties in Modified Lead Titanate Ceramics," (PhD thesis, Pennsylvania State University, 1987).

30. D. J. Taylor, D. Damjanovic, A. S. Bhalla, and L. E. Cross, "Complex Piezoelectric, Elastic, and Dielectric Coefficients of La-Doped 0.93 $Pb(Mg_{1/3}\ Nb_{2/3})O_3$:0.07 $PbTiO_3$ Under DC Bias," *Ferroelectrics Letters Section* 11, no. 1 (1990): 1–9, https://doi.org/10.1080/07315179008200775.

31. A. M. González and C. Alemany, "Determination of the Frequency Dependence of Characteristic Constants in Lossy Piezoelectric Materials," *Journal of Physics D: Applied Physics* 29, no. 9 (1996): 2476–2482, https://doi.org/10.1088/0022-3727/29/9/037.

32. A. Bradesko, "RePiDi: A Procedure for Piezoelectric Ceramic Disc Impedance Analysis in Planar and Thickness Mode," (2025), https://repo.ijs.si/abradesko/repidi.

33. C. Shi, J. Ma, J. Wu, et al., "Coexistence of Excellent Piezoelectric Performance and High Curie Temperature in KNN-Based Lead-Free Piezoelectric Ceramics," *Journal of Alloys and Compounds* 846 (2020): 156245, https://doi.org/10.1016/j.jallcom.2020.156245.

34. O. Tokay and M. Yazıcı, "A Review of Potassium Sodium Niobate and Bismuth Sodium Titanate Based Lead Free Piezoceramics," *Materials Today Communications* 31 (2022): 103358, https://doi.org/10.1016/j.mtcomm.2022.103358.

35. F. Z. Yao, K. Wang, and J. F. Li, "Comprehensive Investigation of Elastic and Electrical Properties of Li/Ta-Modified $(K,Na)NbO_3$ Lead-Free Piezoceramics," *Journal of Applied Physics* 113 (2013): 174105, https://doi.org/10.1063/1.4803711.

36. PI Ceramic GmbH, *Material Data Specific Parameters of Standard Materials* (PI Ceramic GmbH, 2026), https://www.piceramic.com/.

37. J. Zheng, S. Takahashi, S. Yoshikawa, K. Uchino, and J. W. C. de Vries, "Heat Generation in Multilayer Piezoelectric Actuators," *Journal of the American Ceramic Society* 79, no. 12 (1996): 3193–3198, https://doi.org/10.1111/j.1151-2916.1996.tb08095.x.

38. A. Bradeško, *Data for the Manuscript "Microstructural Engineering" of Acceptor-Doped Sodium Potassium Niobate for Enhanced and Temperature-Stable Electromechanical Response* (Zenodo, 2026), https://doi.org/10.5281/zenodo.19201044.

Supporting Information

Additional supporting information can be found online in the Supporting Information section.

Supporting File: ijac70201-sup-0001-SuppMat.docx.